Supplementary Information for "Sleuthing out exotic quantum spin liquidity in the pyrochlore magnet $Ce_2Zr_2O_7$"

Anish Bhardwaj,[1,2,*] Shu Zhang,[3] Han Yan,[4] Roderich Moessner,[5]
Andriy H. Nevidomskyy,[4,†] and Hitesh J. Changlani[1,2,‡]

[1]*Department of Physics, Florida State University, Tallahassee, FL 32306, USA*
[2]*National High Magnetic Field Laboratory, Tallahassee, FL 32310, USA*
[3]*Department of Physics & Astronomy, University of California, Los Angeles, CA, USA*
[4]*Department of Physics & Astronomy, Rice University, Houston, TX 77005, USA*
[5]*Max Planck Institute for Physics of Complex Systems, 01187 Dresden, Germany*

SUPPLEMENTARY NOTE 1: EFFECTIVE HAMILTONIAN: J- AND g-MATRICES

Adopting a notation similar to that used in Supplementary Refs. 1 and 2, the most general nearest-neighbor (nn) Hamiltonian that describes the dipole-octupole system in terms of effective spin-1/2 degrees of freedom (defined in a local basis) is given by,

$$H_{nn} = \sum_{\langle ij \rangle} J_x s_i^x s_j^x + J_y s_i^y s_j^y + J_z s_i^z s_j^z + J_{xz}(s_i^x s_j^z + s_i^z s_j^x) - \sum_i (\hat{z}_i \cdot \mathbf{h})(g_x s_i^x + g_z s_i^z) \quad (1)$$

In this convention s_i^x and s_i^z refer to dipolar degrees of freedom and s_i^y refers to the octupolar degree of freedom on site i. $\langle ij \rangle$ refers to nn pairs of sites. J_x, J_y, J_z and J_{xz} are interaction parameters and g_x and g_z denote coupling strengths of the dipolar degrees to the local z component of $\mathbf{h} = \mu_B \mu_0 \mathbf{H}$, where $\mathbf{H}$ is the applied magnetic field and μ_B is the Bohr magneton. Note that the last term differs from the usual Zeeman coupling of dipoles to an applied magnetic field.

Using sublattice labels $0, 1, 2, 3$, for the four sublattices of the pyrochlore lattice, the local coordinate system at each site is given by,

$$\begin{aligned}
\hat{z}_0 &= \frac{1}{\sqrt{3}}(1,1,1), \quad \hat{y}_0 = \frac{1}{\sqrt{2}}(0,1,-1) \\
\hat{z}_1 &= \frac{1}{\sqrt{3}}(1,-1,-1), \quad \hat{y}_1 = \frac{1}{\sqrt{2}}(-1,0,-1) \\
\hat{z}_2 &= \frac{1}{\sqrt{3}}(-1,1,-1), \quad \hat{y}_2 = \frac{1}{\sqrt{2}}(-1,-1,0) \\
\hat{z}_3 &= \frac{1}{\sqrt{3}}(-1,-1,1), \quad \hat{y}_3 = \frac{1}{\sqrt{2}}(-1,1,0)
\end{aligned} \quad (2)$$

Using a right handed coordinate system, the local $\hat{x}$ axis is given by $\hat{x}_i = \hat{y}_i \times \hat{z}_i$.

In order to compute observables, it is convenient to transform spins in the local basis to the global frame by using the relation,

$$\begin{bmatrix} s_i^x \\ s_i^y \\ s_i^z \end{bmatrix} = R_i \begin{bmatrix} S_i^x \\ S_i^y \\ S_i^z \end{bmatrix}. \quad (3)$$

where R_i represents a rotation matrix on site i, which depends only on the sublattice it belongs to. R_i are given by the expressions,

$$R_0 = \begin{bmatrix} \sqrt{\frac{2}{3}} & -\frac{1}{\sqrt{6}} & -\frac{1}{\sqrt{6}} \\ 0 & \frac{1}{\sqrt{2}} & -\frac{1}{\sqrt{2}} \\ \frac{1}{\sqrt{3}} & \frac{1}{\sqrt{3}} & \frac{1}{\sqrt{3}} \end{bmatrix}, \quad (4a)$$

$$R_1 = \begin{bmatrix} -\frac{1}{\sqrt{6}} & -\sqrt{\frac{2}{3}} & \frac{1}{\sqrt{6}} \\ -\frac{1}{\sqrt{2}} & 0 & -\frac{1}{\sqrt{2}} \\ \frac{1}{\sqrt{3}} & -\frac{1}{\sqrt{3}} & -\frac{1}{\sqrt{3}} \end{bmatrix}, \quad (4b)$$

$$R_2 = \begin{bmatrix} \frac{1}{\sqrt{6}} & -\frac{1}{\sqrt{6}} & -\sqrt{\frac{2}{3}} \\ -\frac{1}{\sqrt{2}} & -\frac{1}{\sqrt{2}} & 0 \\ -\frac{1}{\sqrt{3}} & \frac{1}{\sqrt{3}} & -\frac{1}{\sqrt{3}} \end{bmatrix}, \quad (4c)$$

$$R_3 = \begin{bmatrix} \frac{1}{\sqrt{6}} & \frac{1}{\sqrt{6}} & \sqrt{\frac{2}{3}} \\ -\frac{1}{\sqrt{2}} & \frac{1}{\sqrt{2}} & 0 \\ -\frac{1}{\sqrt{3}} & -\frac{1}{\sqrt{3}} & \frac{1}{\sqrt{3}} \end{bmatrix}. \quad (4d)$$

Using these expressions, the Hamiltonian in Eq. (1) in global basis acquires the form

$$H_{nn} = \sum_{\langle ij \rangle} J_{ij}^{\mu\nu} S_i^\mu S_j^\nu - h^\mu \sum_i g_i^{\mu\nu} S_i^\nu, \quad (5)$$

where μ, ν refer to global Cartesian components x, y, z, and

$$\begin{aligned}
J_{01} &= \begin{bmatrix} J_1 & J_2 & -J_1 \\ J_3 & -J_1 & J_4 \\ -J_4 & -J_1 & -J_3 \end{bmatrix} J_{02} = \begin{bmatrix} -J_1 & J_1 & J_2 \\ J_4 & J_3 & -J_1 \\ -J_3 & -J_4 & -J_1 \end{bmatrix} \\
J_{03} &= \begin{bmatrix} -J_1 & -J_1 & -J_2 \\ J_4 & -J_3 & J_1 \\ -J_3 & J_4 & J_1 \end{bmatrix} J_{12} = \begin{bmatrix} -J_3 & -J_4 & -J_1 \\ J_1 & -J_1 & -J_2 \\ -J_4 & -J_3 & J_1 \end{bmatrix} \\
J_{13} &= \begin{bmatrix} -J_3 & J_4 & J_1 \\ J_1 & J_1 & J_2 \\ -J_4 & J_3 & -J_1 \end{bmatrix} J_{23} = \begin{bmatrix} -J_4 & J_3 & -J_1 \\ -J_3 & J_4 & J_1 \\ J_1 & J_1 & J_2 \end{bmatrix}
\end{aligned} \quad (6)$$

where J_1, J_2, J_3 and J_4 are given by,

$$J_1 = \frac{1}{6}\left(-2J_x + \sqrt{2}J_{xz} + 2J_z\right), \tag{7a}$$

$$J_2 = \frac{1}{3}\left(-2J_x - 2\sqrt{2}J_{xz} - J_z\right), \tag{7b}$$

$$J_3 = \frac{1}{6}\left(J_x - 2\sqrt{2}J_{xz} - 3J_y + 2J_z\right), \tag{7c}$$

$$J_4 = \frac{1}{6}\left(-J_x + 2\sqrt{2}J_{xz} - 3J_y - 2J_z\right). \tag{7d}$$

In a similar way, the g-matrices are given by

$$g_0 = \begin{bmatrix} g_+ & g_- & g_- \\ g_+ & g_- & g_- \\ g_+ & g_- & g_- \end{bmatrix}, \tag{8a}$$

$$g_1 = \begin{bmatrix} g_- & -g_+ & -g_- \\ -g_- & g_+ & g_- \\ -g_- & g_+ & g_- \end{bmatrix}, \tag{8b}$$

$$g_2 = \begin{bmatrix} g_- & -g_- & g_+ \\ -g_- & g_- & -g_+ \\ g_- & -g_- & g_+ \end{bmatrix}, \tag{8c}$$

$$g_3 = \begin{bmatrix} g_- & g_- & -g_+ \\ g_- & g_- & -g_+ \\ -g_- & -g_- & g_+ \end{bmatrix}. \tag{8d}$$

where, $g_+ = \frac{1}{3}(\sqrt{2}g_x + g_z)$ and $g_- = \frac{1}{3}(g_z - \frac{g_x}{\sqrt{2}})$. These expressions for the J and g matrices differ from their more familiar dipolar counterparts in Supplementary Ref. 3.

The dipolar interaction between sites i, j located at positions $\mathbf{r_i}$ and $\mathbf{r_j}$ respectively, is proportionate to

$$\frac{\vec{m}_i \cdot \vec{m}_j - 3(\vec{m}_i \cdot \hat{r}_{ij})(\vec{m}_j \cdot \hat{r}_{ij})}{r_{ij}^3}. \tag{9}$$

where $r_{ij} = |\mathbf{r_i} - \mathbf{r_j}|$ is the distance between sites, $\hat{r}_{ij}$ is the unit vector along $\mathbf{r_i} - \mathbf{r_j}$. $\vec{m}_i$ is the effective magnetic moment,

$$\vec{m}_i = \hat{z}_i(g_z s_i^z + g_x s_i^x). \tag{10}$$

Truncating Eq. (9) to include only next-nearest neighbor terms, (the nearest neighbor pieces can be incorporated into J_x and J_z), the Hamiltonian takes the form,

$$H_{nnn} = \sum_{\langle\langle ij \rangle\rangle} J_{nnn} \begin{bmatrix} s_i^x & s_i^y & s_i^z \end{bmatrix} \begin{bmatrix} g_x^2 & 0 & g_x g_z \\ 0 & 0 & 0 \\ g_x g_z & 0 & g_z^2 \end{bmatrix} \begin{bmatrix} s_j^x \\ s_j^y \\ s_j^z \end{bmatrix}. \tag{11}$$

where $\langle\langle ij \rangle\rangle$ refers to next nearest neighbors (nnn) on the pyrochlore lattice and J_{nnn} is the strength of the effective interactions.

In the global basis, Eq. (11) takes the form

$$H_{nnn} = \sum_{\langle\langle ij \rangle\rangle} J_{n_{ij}}^{\mu\nu} S_i^\mu S_j^\nu. \tag{12}$$

where $J_{n_{ij}}$ have the form,

$$J_{n01} = \begin{bmatrix} -J_{n_1} & -J_{n_3} & J_{n_1} \\ J_{n_2} & J_{n_1} & -J_{n_2} \\ J_{n_2} & J_{n_1} & -J_{n_2} \end{bmatrix} \tag{13a}$$

$$J_{n02} = \begin{bmatrix} J_{n_1} & -J_{n_1} & -J_{n_3} \\ -J_{n_2} & J_{n_2} & J_{n_1} \\ -J_{n_2} & J_{n_2} & J_{n_1} \end{bmatrix} \tag{13b}$$

$$J_{n03} = \begin{bmatrix} J_{n_1} & J_{n_1} & J_{n_3} \\ -J_{n_2} & -J_{n_2} & -J_{n_1} \\ -J_{n_2} & -J_{n_2} & -J_{n_1} \end{bmatrix} \tag{13c}$$

$$J_{n12} = \begin{bmatrix} -J_{n_2} & J_{n_2} & J_{n_1} \\ -J_{n_1} & J_{n_1} & J_{n_3} \\ J_{n_2} & -J_{n_2} & -J_{n_1} \end{bmatrix} \tag{13d}$$

$$J_{n13} = \begin{bmatrix} -J_{n_2} & -J_{n_2} & -J_{n_1} \\ -J_{n_1} & -J_{n_1} & -J_{n_3} \\ J_{n_2} & J_{n_2} & J_{n_1} \end{bmatrix} \tag{13e}$$

$$J_{n23} = \begin{bmatrix} J_{n_2} & J_{n_2} & J_{n_1} \\ -J_{n_2} & -J_{n_2} & -J_{n_1} \\ -J_{n_1} & -J_{n_1} & -J_{n_3} \end{bmatrix} \tag{13f}$$

where J_{n_1}, J_{n_2} and J_{n_3} have been defined as,

$$J_{n_1} = \frac{J_{nnn}}{6}\left(2g_x^2 - \sqrt{2}g_x g_z - 2g_z^2\right), \tag{14a}$$

$$J_{n_2} = \frac{J_{nnn}}{6}\left(g_x^2 - 2\sqrt{2}g_x g_z + 2g_z^2\right), \tag{14b}$$

$$J_{n_3} = \frac{J_{nnn}}{3}\left(2g_x^2 + 2\sqrt{2}g_x g_z + g_z^2\right). \tag{14c}$$

SUPPLEMENTARY NOTE 2: FINITE TEMPERATURE LANCZOS METHOD

In the finite temperature Lanczos method (abbreviated as FTLM, see Supplementary Ref. 5 for details) the expectation value of any operator (A) is evaluated using the expressions,

$$\langle A \rangle = \frac{N_{st}}{ZR}\sum_{r=1}^{R}\sum_{j=0}^{M} e^{-\beta\epsilon_j^r}\langle r|\psi_j^r\rangle\langle\psi_j^r|A|r\rangle, \tag{15a}$$

$$Z = \frac{N_{st}}{R}\sum_{r=1}^{R}\sum_{j=0}^{M} e^{-\beta\epsilon_j^r}|\langle r|\psi_j^r\rangle|^2. \tag{15b}$$

where N_{st} is the dimension of the entire Hilbert space, Z is the partition function and $\beta = 1/k_B T$ is the inverse temperature. $|r\rangle$ is the initial random state, R denotes the number of such starting states, and $M+1$ is the dimension of the Krylov space spanned by the vectors $|r\rangle$, $H|r\rangle$, $H^2|r\rangle$,...,$H^M|r\rangle$. $|\psi_j^r\rangle$ and ϵ_j^r represent (respectively) the j^{th}Ritz eigenvector and eigenvalue obtained by diagonalizing the Hamiltonian in the Krylov space.

To evaluate the expectation value of the observables accurately the convergence with respect to both R and

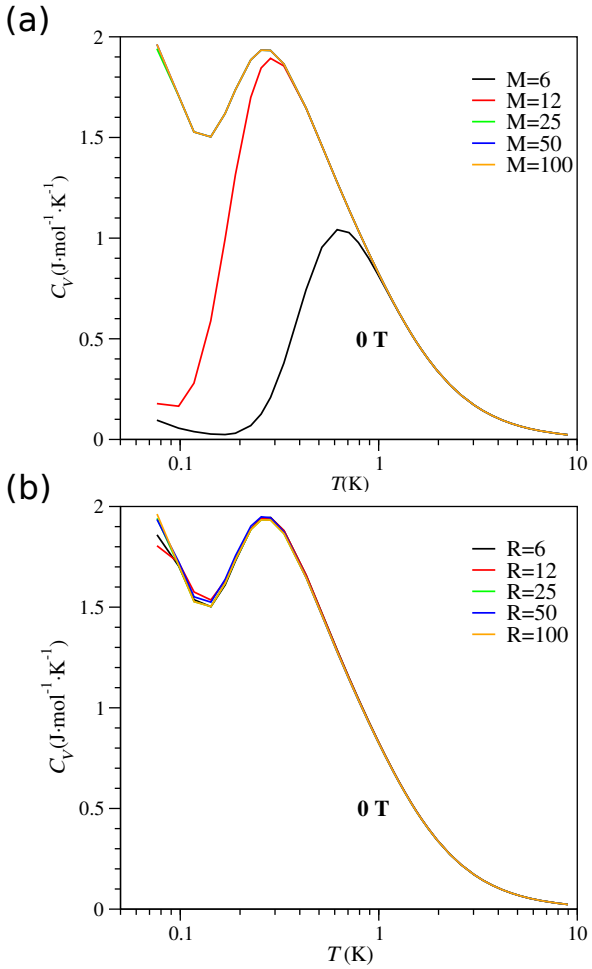

Supplementary Figure 1. Panel (a) shows the variation of the specific heat profile at zero field with M for $R = 100$ in the finite temperature Lanczos method (FTLM). Panel (b) shows the variation of the specific heat profile with R for $M = 50$. The Hamiltonian parameters for both panels correspond to set no. 2 (see Supplementary Table 1).

M was checked (see Supplementary Fig. 1 for a representative example and see previous work in Supplementary Ref. 6). The specific heat was evaluated using Eq. (15a) to compute $\langle H\rangle$ and $\langle H^2\rangle$ and using the expression,

$$C_V = \frac{1}{k_B T^2}\left(\langle H^2\rangle - \langle H\rangle^2\right). \tag{16}$$

Similarly, the magnetization was evaluated by calculating the free energy

$$F = -k_B T \ln Z \tag{17}$$

and then taking its derivative with respect to the field strength.

SUPPLEMENTARY NOTE 3: PARAMETER FITTING

We devise a cost function involving the weighted errors between the experimental data (taken from Supplementary Ref. 4) and the numerically computed observables for a given Hamiltonian parameter set. We use the specific heat which is known for different values of temperature and magnetic field strength h and the magnetization along the [111] direction, and define,

$$f = \alpha_c \sum_j \sqrt{\frac{\sum_{i=1}^{N_c}(C_V^e(T_i,h_j) - C_V^s(T_i,h_j))^2}{N_c}} + \alpha_m \sum_j \sqrt{\frac{\sum_{i=1}^{N_m}(M^e(T_j,h_i) - M^s(T_j,h_i))^2}{N_m}} \tag{18}$$

where C_V^e, C_V^s are the specific heat and M^e, M^s are the magnetization along the [111] direction from experiment (taken from Supplementary Ref. 4) and FTLM simulations respectively. N_c and N_m are the number of data points for the specific heat and magnetization respectively. α_c, α_m are weight factors. For example, in situations where only specific heat fitting was of interest $\alpha_c = 1$, $\alpha_m = 0$. When discussing our various strategies, we specify what regimes of the experimental data were retained for the fitting procedure or for computing the cost function.

It should be emphasized that minimizing the cost function in Eq. (18) without constraining the domain of each parameter can yield unphysical values. Additionally, given that the phase space spanned by the six parameters entering Eq. (1) is large, it can be time consuming to yield a physical solution. It is imperative that the optimization be performed by imposing bounds on each parameter.

These parameter bounds were found by noting that the specific heat curves for $Ce_2Zr_2O_7$ show no sharp anomaly at low temperature and the zero field specific heat has a Schottky like bump only for scales less than 0.3 K. This sets an approximate upper bound for the interaction strengths at around 0.10 meV. For temperatures much larger than the energy scale of the interaction strength, the system can be essentially regarded as a non-interacting one. Utilizing this observation, we were able to describe the magnetization curves at 1.8 K and 4 K (both of which are larger than the expected interaction strengths) using just the single ion magnetic field term in the Hamiltonian in Eq. (1).

This was achieved by setting $g_x = 0$ and $g_z \approx 2.4$. It was found that while this particular combination of g_x and g_z, works very well to describe the high temperature magnetization curves, it was not so accurate in describing the low temperature magnetization at 0.5 K especially at higher values of field strength. (A closer

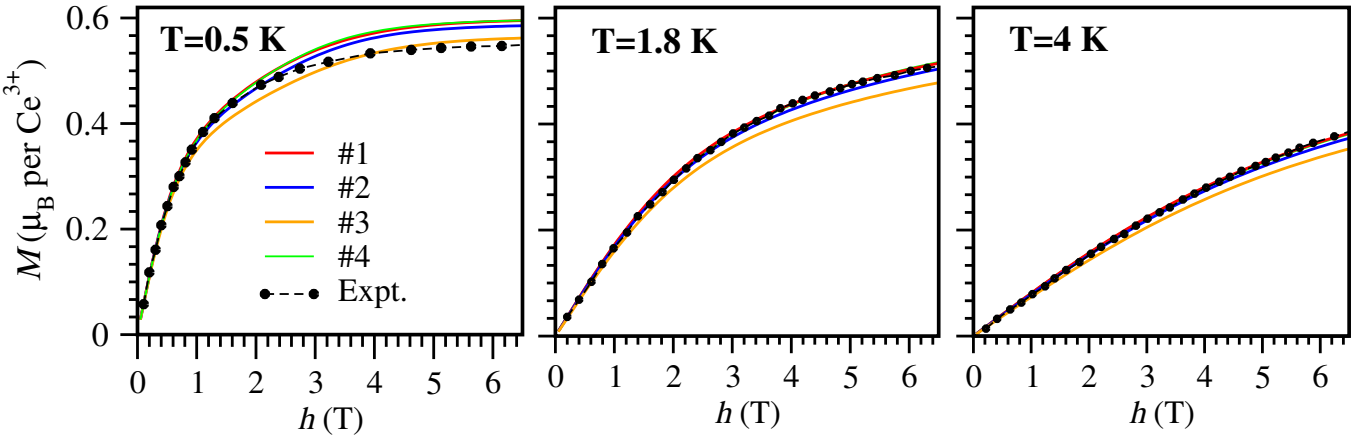

Supplementary Figure 2. Magnetization (M) vs field strength (h) for the [111] direction at temperatures of 0.5 K, 1.8 K and 4.0 K. The solid black circles connected by dashed lines represent the experimental data (extracted from 4), the red, blue, orange and green solid lines represent the results from FTLM by using parameter set 1, 2, 3, and 4 respectively (see Supplementary Table 1). The green and red curves visually overlap each other.

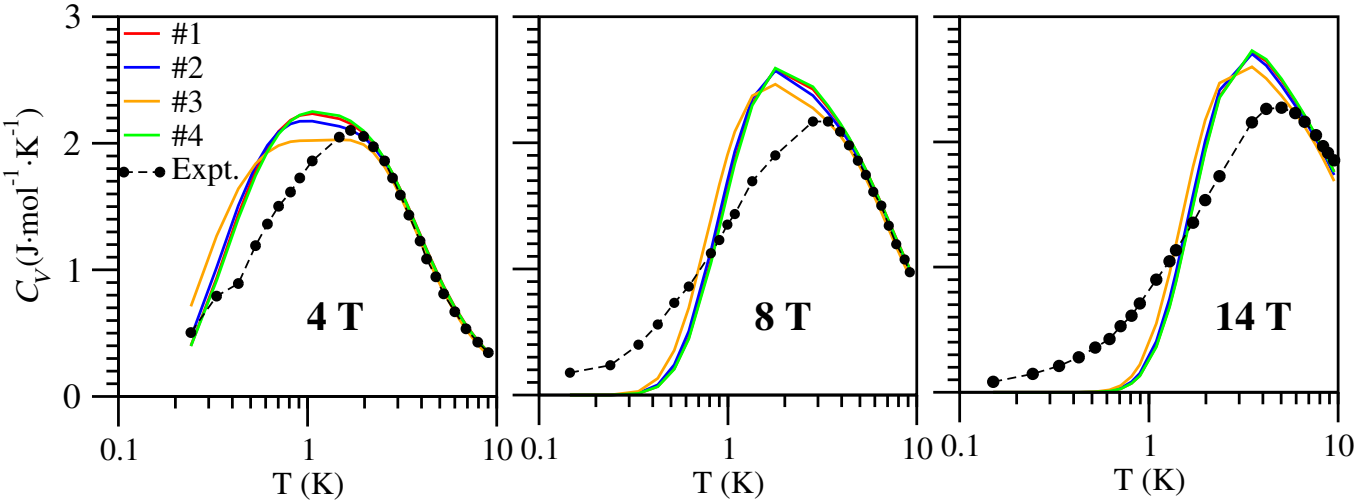

Supplementary Figure 3. Specific heat vs. temperature for four Hamiltonian parameter sets (shown in Supplementary Table 1) as compared to experiment for field strengths of 4 T, 8 T and 14 T applied along the [111] direction. The experimental data was extracted from Supplementary Ref. 4.

look at the report of Supplementary Ref. 4 suggests a g_z value that is changing with magnetic field, an effect not built into our model). Besides this set, we also noticed that the set $g_z \sim 2.35$ and $g_x \sim -0.2324$, which can describe the various magnetization curves reasonably well, has slightly better accuracy while describing the low temperature magnetization curve. This gain in accuracy comes at the cost of a small loss in accuracy when describing the high temperature magnetization curves.

After having found estimates for the g parameters, we minimize the cost function in Eq. (18) using a 16 site pyrochlore system by allowing the interaction parameters to vary between different bounds and different initial starting parameters. For this we employed the SLSQP algorithm in the SciPy package. The end results of our investigations yield multiple sets of optimized parameters, they are summarized in Supplementary Table 1. Some representative results for these parameter sets are presented in Supplementary Fig. 2 and Supplementary Fig. 3. Many features of the data of Supplementary Ref. 4 are captured correctly, especially in the high temperature and low magnetic field strength regime.

We discuss some more specifics associated with the fitting procedure and the parameter sets. Parameter set 1 was obtained by fixing g_x and g_z to 0 and 2.401 respectively and optimizing the J_x, J_y, J_z and J_{xz} to fit only the specific heat curves ($\alpha_c = 1$ and $\alpha_m = 0$). Parameter set 2 was obtained by fixing g_x, g_z and J_{xz} to -0.2324,

Set	J_1	J_2	J_3	J_4	g_x	g_z	J_x	J_y	J_z	J_{xz}
parameter set 1	-0.009	-0.035	-0.031	-0.056	0	2.401	0.044	0.087	0.015	0
parameter set 2	-0.006	-0.032	-0.030	-0.057	-0.2324	2.35	0.0385	0.088	0.020	0
parameter set 3	-0.004	-0.036	-0.024	-0.056	0.574	2.196	0.041	0.081	0.027	0
parameter set 4	-0.018	-0.05	-0.018	-0.049	0.0	2.4	0.069	0.068	0.013	0

Supplementary Table 1. Parameter sets studied in the paper. All J values are in meV units, and all g values are dimensionless

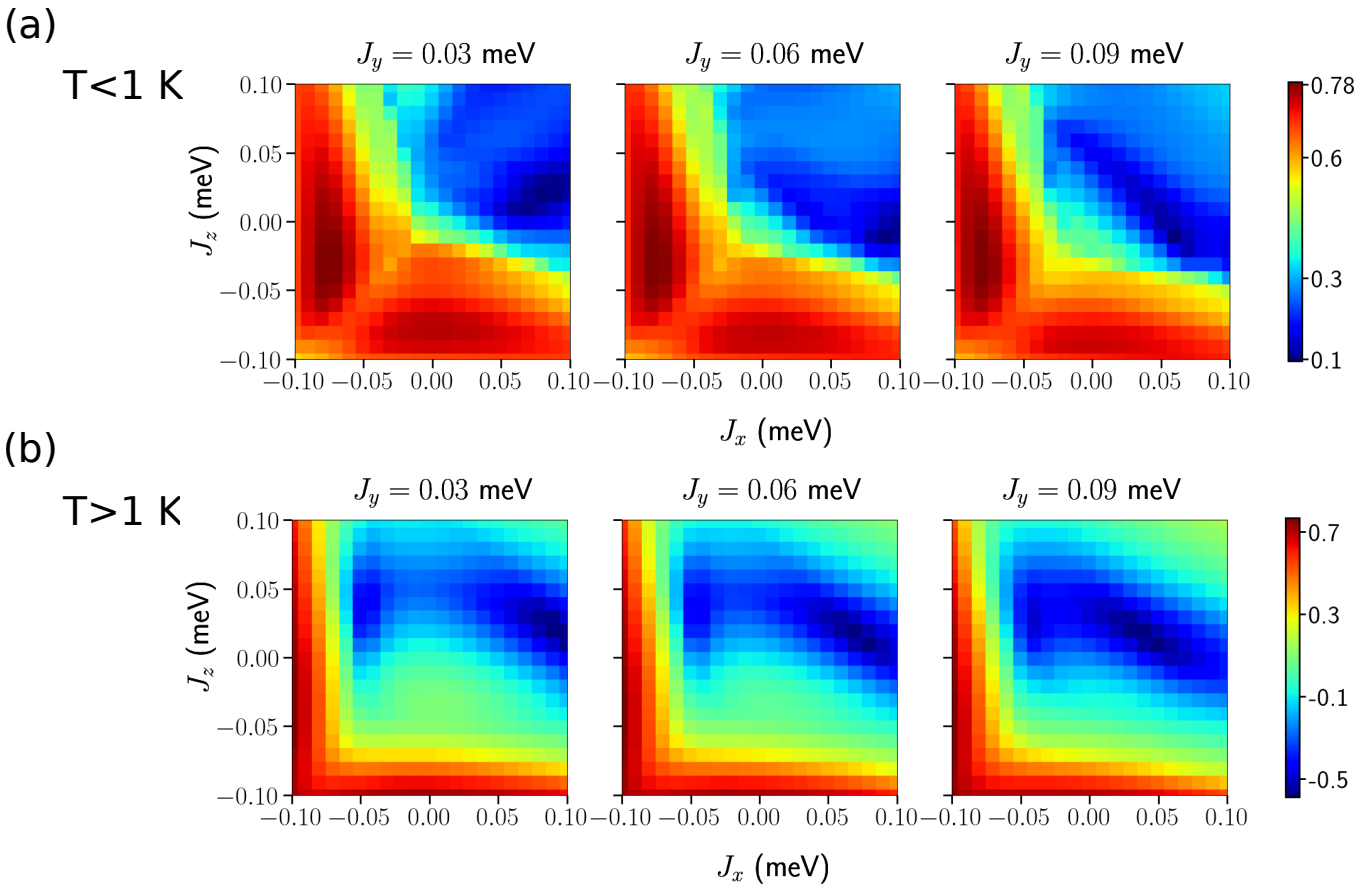

Supplementary Figure 4. Two dimensional $J_x - J_z$ cross sections of the cost function for fixed J_y-values 0.03, 0.06 and 0.09 meV. (a) was obtained by using the low temperature part ($T < 1$ K) of the specific heat curves in the cost function and (b) was obtained by using their high temperature part ($T > 1$ K). The colors represent the log of the cost function.

2.35 and 0 respectively and then optimizing the J_x, J_y, J_z to fit the specific heat curves ($\alpha_c = 1$ and $\alpha_m = 0$). On the other hand, parameter set 3 was obtained by fixing J_{xz} to zero and optimizing everything else to fit both the specific heat and the $T = 0.5$ K magnetization curve with field along the [111] direction ($\alpha_c = 1$ and $\alpha_m = 1$). Parameter set 4 was obtained fixing J_{xz} g_x and g_z to zero, zero and 2.4 respectively and optimizing everything else to fit both the specific heat and the $T = 0.5$ K magnetization curve with field along the [111] direction. All optimizations were performed using only the high temperature part ($T > 1$ K) of the specific heat curves.

In order to build confidence in our optimized parameters, we also performed a brute force scan in a restricted part of parameter space. We mapped out the cost function for the specific heat ($\alpha_c = 1$, $\alpha_m = 0$) by varying J_x, J_y and J_z from -0.1 to 0.1 meV in steps of 0.01 meV, while keeping $J_{xz} = 0$, $g_x = 0$ and $g_z = 2.4$. Note that for $g_x = J_{xz} = 0$, all properties of the Hamiltonian (including specific heat and magnetization) are invariant to exchanging x and y. Thus the cost function for a set (J_x, J_y, J_z) is identical to that for (J_y, J_x, J_z).

In Supplementary Fig. 4 we present a few representative cross-sections of the cost-function map keeping J_y fixed and varying J_x. In these maps, the colors correspond to the log of the cost function. The figures were constructed including either only the low temperature data ($T < 1$ K, Supplementary Fig. 4a) or only the high

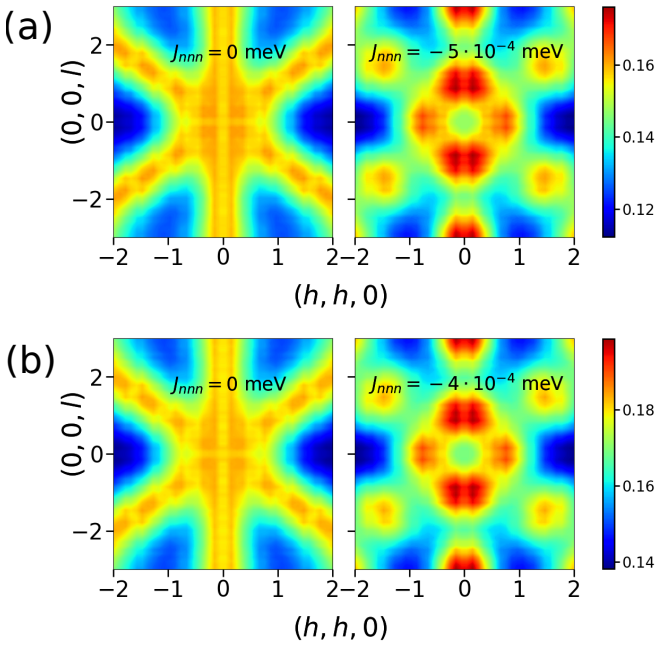

Supplementary Figure 5. Panels (a) and (b) show the (projected) static spin structure factor, obtained by classical Monte Carlo simulation, for parameter set 2 and 4 respectively (see Supplementary Table 1). The simulation was performed using 8192 sites and 10^6 Monte Carlo sweeps.

temperature data ($T > 1$ K, Supplementary Fig. 4b) for the evaluation of the cost function. Our parameter sets with $g_x = 0$ and $g_z = 2.4$, which have been obtained using full optimization ($\alpha_c = \alpha_m = 1$), lie in the dark blue region of the cost map shown in Supplementary Fig. 4b.

We observe that in addition to the solutions obtained by using the optimizer, the cost map suggests existence of other promising sets. This happens because of the $x - y$ symmetry mentioned above. It should be emphasized that this symmetry is only present when g_x and J_{xz} are both zero. In practice, we observed that allowing for a non-zero g_x in the optimization selects the $J_y > J_x$ set.

The optimization procedure also yielded parameter sets which were discarded because their low temperature ($T < 1$ K) cost function of specific heat at zero field was large (when compared against the sets mentioned in Supplementary Table 1). Some of these discarded parameter sets have the following interaction strengths (in meV): (a) $J_x = -0.036$, $J_y = -0.035$ $J_z = 0.032$ and $J_{xz} = 0$ (b) $J_x = -0.043$, $J_y = 0.084$, $J_z = 0.02$ and $J_{xz} = 0$ (c)$J_x = 0.085$, $J_y = -0.043$, $J_z = 0.038$ and $J_{xz} = 0$. All our optimizations, using both specific heat and magnetization (both low and high temperature), involving J_x, J_y, J_z and g_z (with $J_{xz} = 0$ and $g_x = 0$) yielded $g_z \sim 2.2$. Such parameter sets, where $g_z \sim 2.2$ are less reliable as they are unable to explain the magnetization curves accurately at higher temperature (see parameter set 3 in Supplementary Fig. 2).

As mentioned in the main text, H_{nn} alone is insufficient to explain the INS data, at least at the level of a classical treatment of the Hamiltonian. We find that classical Monte Carlo and SCGA calculations of H_{nn} along with a suitably chosen J_{nnn} that enters H_{nnn} (the truncated dipolar interaction discussed earlier in Supplementary Note 1), are in reasonable agreement with the INS data. In Supplementary Fig. 5, we show the static structure factor (to be discussed in Supplementary Note 5) corresponding to what is measured in INS. We provide results for Hamiltonian parameter set 2 and 4 both with and without H_{nnn}. Since parameter set 1 and 3 are close to parameter set 2, the static structure factor for these sets are also qualitatively similar, and hence not shown.

SUPPLEMENTARY NOTE 4: FINITE SYSTEM SIZE EFFECTS

We comment here on the finite size dependence of the specific heat and magnetization by using parameter set no. 2. In Supplementary Fig. 6 and Supplementary Fig. 7 we show the specific heat and magnetization, respectively, obtained by full diagonalization or FTLM for 4 (single tetrahedron), 16 and 32 site systems. We clearly observe that the magnetization is less sensitive to system size compared to the specific heat. At higher temperatures, however, both magnetization and specific heat show smaller variations with system size suggesting that even a small system is sufficient to explain the high temperature properties.

SUPPLEMENTARY NOTE 5: STATIC AND DYNAMIC STRUCTURE FACTOR

We now discuss further details of our classical static and dynamical calculations. We work in the global x, y, z basis and evaluate the equal time (static) expectation values,

$$S(\mathbf{q}) = \frac{1}{N}\sum_{\mu\nu}\left(\delta_{\mu\nu} - \frac{q_\mu q_\nu}{q^2}\right)\langle m^\mu(-\mathbf{q}) m^\nu(\mathbf{q})\rangle \quad (19a)$$

$$m^\mu(\mathbf{q}) = \sum_i e^{-i\mathbf{q}\cdot\mathbf{r}_i}\sum_\lambda g_i^{\mu\lambda} S_i^\lambda \quad (19b)$$

where N is the number of sites. We use classical Monte Carlo and employ the standard Metropolis algorithm with continuous conical moves to sample spin configurations. We perform N single spin moves (collectively referred to as a sweep) between two measurements.

For dynamical properties, we use the molecular dynamics (MD) procedure. In this method, N_{IC} equilibrium configurations were first drawn from the thermal ensemble at $T = 0.06$ K using classical Monte Carlo, then each of these initial configurations (IC) were evolved in time by using the Landau-Lifshitz equation,

$$\frac{d\mathbf{S_i}}{dt} = \mathbf{S_i} \times \mathbf{h_{eff,i}} \quad (20)$$

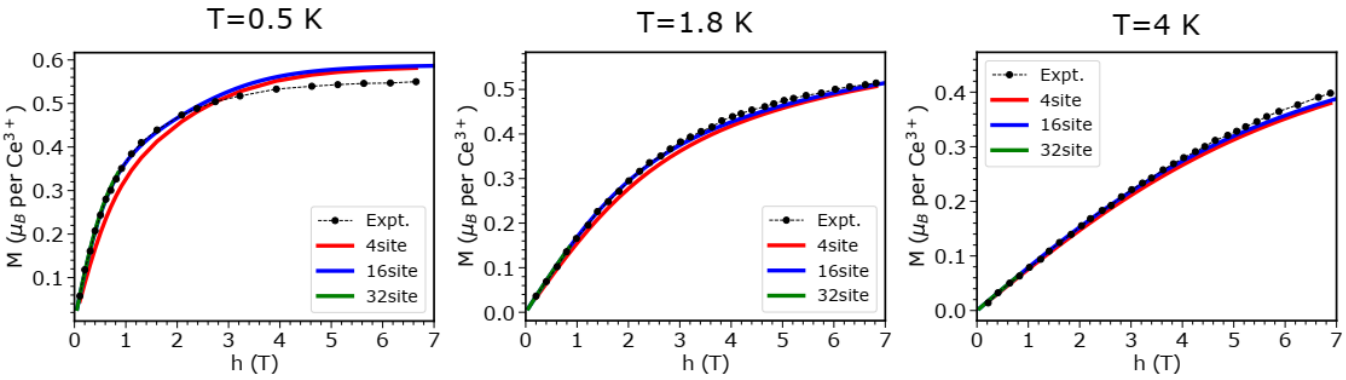

Supplementary Figure 6. Magnetization along the same direction as applied field ([111]), obtained by FTLM, for different system sizes for parameter set no. 2. For 32 sites, FTLM was performed by using only a single seed and magnetization values have been shown upto 1 T field.

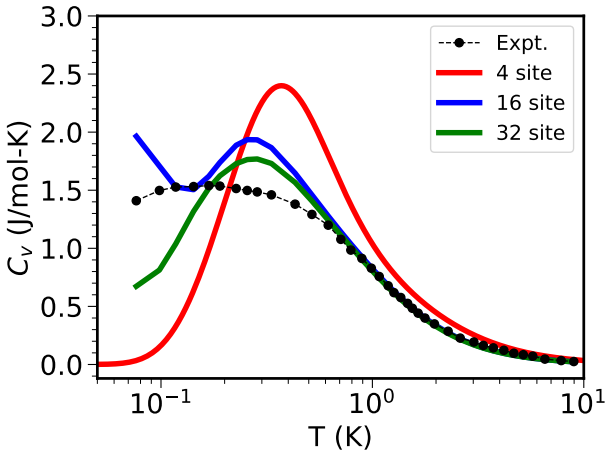

Supplementary Figure 7. Specific heat (for the case of no applied magnetic field), obtained by FTLM, for different system sizes for parameter set no. 2. For 32 sites, FTLM was performed by using only a single seed ($R = 1$).

where $\mathbf{h_{eff,i}}$ is the effective magnetic field (local exchange field) experienced by a spin at site i, due to the interactions with all other spins it is coupled to. The time evolution of spins given by Eq. (20) is performed numerically using the fourth order Runge-Kutta method (see Supplementary Ref. 7–9). A sufficiently small time step was chosen to ensure that the energy was (roughly) constant with time. The evolution was done for a total time of $T_s = 500$ meV^{-1}.

To compare with what is measured in the INS experiment, we first calculate the appropriately projected dynamical structure factor for each IC (which we refer to as $S^{IC}(\mathbf{q},\omega)$) and average it over N_{IC} configurations:

$$S^{IC}(\mathbf{q},\omega) = \frac{T_s}{\pi N}\sum_{\mu\nu}\left(\delta_{\mu\nu} - \frac{q_\mu q_\nu}{q^2}\right)\langle m^\mu(-\mathbf{q},-\omega)m^\nu(\mathbf{q},\omega)\rangle \tag{21a}$$

$$m^\mu(\mathbf{q},\omega) = \frac{1}{T_s}\int_0^{T_s} dt\; e^{i\omega t}\sum_i e^{-i\mathbf{q}\cdot\mathbf{r}_i}\sum_\lambda g_i^{\mu\lambda}S_i^\lambda \tag{21b}$$

We then use the quantum-classical correspondence discussed in Supplementary Ref. 9 to obtain $S_{quantum}(\mathbf{q},\omega) \equiv \beta\omega S(\mathbf{q},\omega)$

SUPPLEMENTARY NOTE 6: ENHANCED SPECTRAL WEIGHT AT $X = (0,0,1)$

In the main text we showed color plots for energy vs. momentum for one dimensional cross sections in momentum space. The corresponding E vs l plot from the experiment depicts an enhanced spectral weight at $X = (0,0,1)$. Fig. 1d in the main text shows that our MD simulation also captures this feature. To further bolster this assertion we present in Supplementary Fig. 8 two different line-cuts at energies $E = 0.01$ meV and $E = 0.03$ meV where the intensity maximum at the X point can be clearly perceived.

SUPPLEMENTARY NOTE 7: IMPORTANCE OF J_y

For most parameter sets, in particular set no. 2 (see Supplementary Table 1) which was used for the calculations in the main text, we observe that J_y is the dominant interaction term. To assess its importance, we evaluate

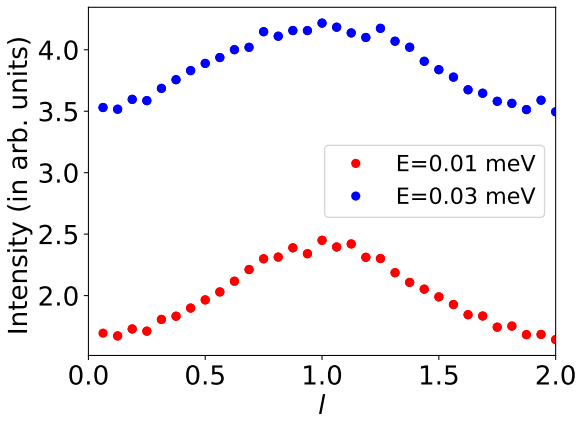

Supplementary Figure 8. Calculated intensity (projected dynamical structure factor) vs. momentum for the (00l) cross section, from classical MD simulations at $T = 0.06$ K for energies 0.01 meV and 0.03 meV. Enhanced spectral weight at $X = (0, 0, 1)$ is seen.

the specific heat and magnetization by using this parameter set with J_y set to zero. The final result obtained has been compared with experiment, see Supplementary Fig. 9. We observe that the specific heat in zero applied field, obtained from parameter set no. 2 with J_y set to zero, is unable to describe the experiment at higher values of temperature. We also observe that the [111] magnetization at 0.5 K obtained with $J_y = 0$ is less accurate at lower magnetic field strengths.

SUPPLEMENTARY NOTE 8: EFFECTIVE HAMILTONIAN FOR A π-FLUX OCTUPOLAR SPIN LIQUID

In this section we briefly explain how the parameters of Supplementary Table 1 place the model in the phase of $\pi-$flux octupolar quantum spin ice, and we also clarify the precise meaning of "$\pi-$flux".

For $J_{xz} = 0$ and no external magnetic field, the nn Hamiltonian in the local basis is written as

$$\mathcal{H} = \sum_{ij} \left[J_y s_i^y s_j^y + J_x s_i^x s_j^x + J_z s_i^z s_j^z \right]. \tag{22}$$

We note that for three out of our four parameter sets $J_y > J_x,\ J_z > 0$. Inspired by this observation, we treat the term $J_y s_i^y s_j^y$ as the dominant one. This enforces the "2-in-2-out" ice rule on each tetrahedron for the local s^y components. Since s^y is of octupolar nature, the large J_y places the system in the octupolar ice phase. The other terms $J_x s_i^x s_j^x + J_z s_i^z s_j^z$ introduce quantum dynamics to the octupolar ice states, we will take them to be small enough that perturbative arguments apply. We can rewrite them in terms of the raising and lowering operators of s^y

$$s^{y+} = s^z + i s^x, \quad s^{y-} = s^z - i s^x. \tag{23}$$

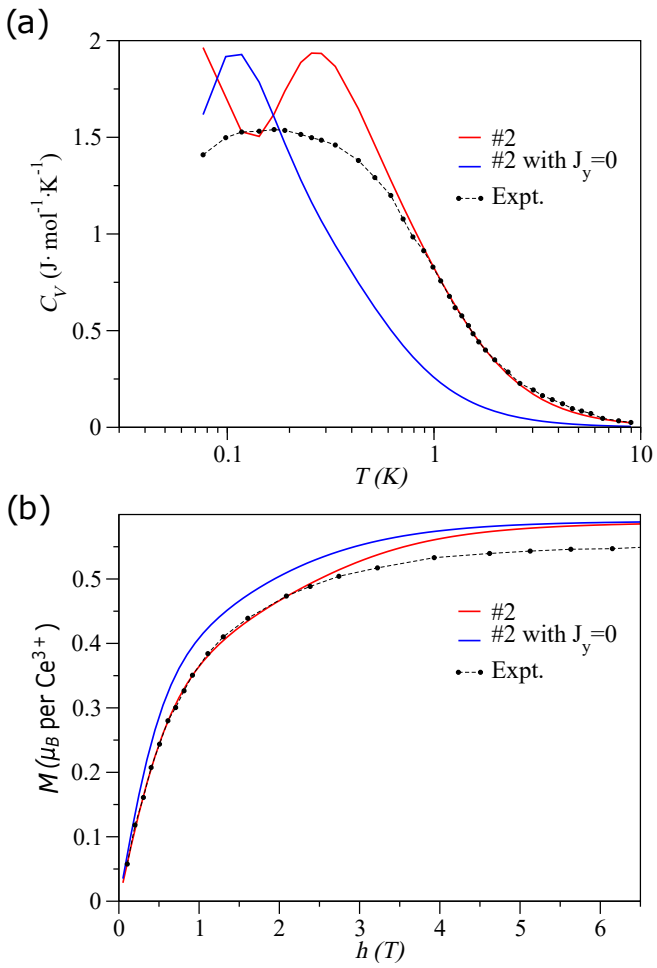

Supplementary Figure 9. (a) Comparison of the specific heat vs. temperature profile at zero field obtained by using parameter set 2 (red), parameter set 2 with J_y set to zero (blue) and the experiment (black solid circles connected by dashed lines). (b) Magnetization vs. magnetic field along the [111] direction at 0.5 K. The FTLM calculations were performed for a 16 site cluster.

The Hamiltonian then becomes

$$\mathcal{H} = \sum_{ij} \Bigg[J_y s_i^y s_j^y + \frac{J_z + J_x}{4} (s_i^{y+} s_j^{y-} + s_j^{y+} s_i^{y-}) + \frac{J_z - J_x}{4} (s_i^{y+} s_j^{y+} + s_j^{y-} s_i^{y-}) \Bigg]. \tag{24}$$

where

$$0 < \frac{J_z + J_x}{4} \ll J_y, \quad \frac{J_x - J_z}{4} \ll \frac{J_z + J_x}{4}. \tag{25}$$

If we ignore the term with the smallest coefficient $\frac{J_x - J_z}{4}$, the rest of the Hamiltonian becomes identical to that of regular quantum spin ice model, and has been studied in detail. The term $\frac{J_z + J_x}{4}(s_i^{y+} s_j^{y-} + s_j^{y+} s_i^{y-})$ flips two neighbouring spins. When restricted to the "2-in-2-out" ice state Hilbert space, it perturbatively generates

the loop exchange term. The lowest order one is defined on hexagons of the pyrochlore lattice as

$$H_{\rm flux} = J_{\rm ring} \sum_{\hexagon} \cos(\nabla_{\hexagon} \times A), \tag{26}$$

where $J_{\rm ring} \sim (J_x + J_z)^3/(64 J_y^2)$ is positive. Here the term $\cos(\nabla_{\hexagon} \times A)$ refers to the spin flipping operators $s_1^+ s_2^- s_3^+ s_4^- s_5^+ s_6^-$ on a hexagon.

The quantum dynamical terms are believed to lead the system into a quantum spin ice phase (see Supplementary Ref. 10 and 11). Furthermore, the positive $J_{\rm ring}$ favors the ground state, at the mean-field level, to satisfy $\cos(\nabla_{\hexagon} \times A) = -1$ on each hexagon, which is referred to as the $\pi-$flux state. This ground state is qualitatively different from the $0-$flux phase favoured by $\cos(\nabla_{\hexagon} \times A) = 1$. In the $\pi-$flux state, the mean-field ansatz of gauge fields is not trivially $A = 0$ but a more complex pattern (see Supplementary Ref. 11), and leads the system into a different quantum spin ice phase than that of $A = 0$ background. More detailed studies of the $\pi-$flux phase can be found in Supplementary Refs. 2, 11–13.

The $\pi-$flux quantum spin ice is expected to be more stable than the $0-$flux quantum spin ice. Crudely speaking, this is because positive $J_{x,y,z}$ creates more frustration than just one positive J_y, and stabilizes the phase to a large region of the parameter space. Thus, turning on the small $\frac{J_z - J_x}{4}(s_i^{y+} s_j^{y+} + s_j^{y-} s_i^{y-})$ term does not qualitatively affect the physics, as shown in the phase diagram in Supplementary Ref. 2.

SUPPLEMENTARY NOTE 9: SINGLE ION PHYSICS

For a single electron in the presence of uniform magnetic field, the leading order interaction (in orders of field strength h), is the Zeeman term given by,

$$H_Z = -\mathbf{h} \cdot (\mathbf{L} + \mathbf{2S}). \tag{27}$$

We choose our local quantization axis (z) to be along the local [111] direction, identical to the choice in Eq. (2). Throughout this section we use J_x, J_y and J_z to represent the x, y and z component of the total angular momentum $\mathbf{J} = \mathbf{L} + \mathbf{S}$, not to be confused with the exchange parameters J_x, J_y and J_z that appear in the Hamiltonian in the rest of the paper.

When the ground state is well-isolated from the excited states, the low energy physics of the ion can be captured by expressing the above Hamiltonian in the subspace spanned by the lowest lying multiplet. Here, we discuss two cases, namely (a) the ground state is a doublet which is given $J = 5/2$ and $J_z = \pm 3/2$ and (b) the ground state is a doublet which is a particular linear combination of the $J = 5/2$ and $J = 7/2$ states.

Ground state doublet is $|J = 5/2,\ J_z = \pm 3/2\rangle$

We first consider the case where the ground state doublet is

$$|\pm\rangle = |5/2, \pm 3/2\rangle. \tag{28}$$

We treat the term mentioned in Eq. (27) as a perturbation and find its matrix elements in the $|\pm\rangle$ subspace. To do so, we make use of a result that follows from the Wigner-Eckart theorem (see Supplementary Ref. 14), which states that the matrix element of any vector operator in the eigenstates of $\mathbf{J^2}$ and J_z with a given J is proportional to the matrix element of $\mathbf{J}$ itself.

$$\langle J, J_z | \mathbf{L} + \mathbf{2S} | J, J_z' \rangle = g(JLS) \langle J, J_z | \mathbf{J} | J, J_z' \rangle. \tag{29}$$

where,

$$g(JLS) = \frac{3}{2} + \frac{1}{2}\left[\frac{S(S+1) - L(L+1)}{J(J+1)}\right]. \tag{30}$$

Clearly, $\langle \pm | \mathbf{L} + \mathbf{2S} | \mp \rangle = 0$ and only the diagonal elements contribute. For the diagonal elements we note that only the z-component of the vector of matrix elements $\langle + | \mathbf{L} + \mathbf{2S} | + \rangle$ is non-zero. This means

$$\begin{aligned} \mathbf{h} \cdot \langle + | \mathbf{L} + \mathbf{2S} | + \rangle &= h_z \langle + | L_z + 2S_z | + \rangle \\ &= h_z g(JLS) \langle + | J_z | + \rangle. \end{aligned} \tag{31}$$

The matrix element $\mathbf{h} \cdot \langle - | \mathbf{L} + \mathbf{2S} | - \rangle$ can be evaluated in a similar way, and thus the Zeeman term in the $|\pm\rangle$ basis takes the form,

$$H_Z = -h_z g_z s_z. \tag{32}$$

where $s_z = \frac{\sigma_z}{2}$ is a an effective spin-1/2 operator and σ_z is the usual 2×2 Pauli matrix.

Ground state doublet is a linear combination of $J = 5/2$ and $J = 7/2$

For the isostructural compound $Ce_2Sn_2O_7$, Supplementary Ref. 15 has determined that the ground state doublet, after including the $J = 7/2$ manifold, for a single Cerium ion in the presence of spin-orbit coupling and crystal field is,

$$\begin{aligned} |\pm\rangle = 0.87 |^2F_{5/2}, \pm 3/2\rangle \pm 0.46 |^2F_{5/2}, \mp 3/2\rangle \\ \mp 0.15 |^2F_{7/2}, \pm 3/2\rangle - 0.01 |^2F_{7/2}, \mp 3/2\rangle. \end{aligned} \tag{33}$$

We note that Supplementary Ref. 4 has not reported any such mixing for the case of $Ce_2Zr_2O_7$. We allow for such a possibility for $Ce_2Zr_2O_7$, and leave the precise determination of the wavefunction coefficients to future experiments. Instead we will use the numbers appearing in Eq. (33) simply to motivate the form of the Zeeman term in the subspace of this doublet. The exercise will illustrate how a non-zero g_x can possibly emerge.

Clearly, Eq. (29) can no longer be used to evaluate the matrix element of the type

$\langle {}^2F_{5/2}, \pm 3/2|\mathbf{L}+\mathbf{2S}|{}^2F_{7/2}, \pm 3/2\rangle$ as the J-values on the left and right are different. To evaluate these matrix elements we first define,

$$|1\rangle \equiv |{}^2F_{5/2}, 3/2\rangle, \tag{34a}$$
$$|2\rangle \equiv |{}^2F_{5/2}, -3/2\rangle, \tag{34b}$$
$$|3\rangle \equiv |{}^2F_{7/2}, 3/2\rangle, \tag{34c}$$
$$|4\rangle \equiv |{}^2F_{7/2}, -3/2\rangle. \tag{34d}$$

It is easy to observe that

$$\langle i|L_\alpha + 2S_\alpha|j\rangle = 0, \quad i,j \,\epsilon\, (1,2,3,4), \quad \alpha \,\epsilon\, (x,y). \tag{35}$$

so that the only terms to be evaluated are $\langle i|L_z+2S_z|j\rangle$. It can also be shown that $\langle 1|L_z + 2S_z|2\rangle = \langle 1|L_z + 2S_z|4\rangle = \langle 2|L_z + 2S_z|3\rangle = \langle 3|L_z + 2S_z|4\rangle = 0$. The remaining combinations can be evaluated by using 8 different Clebsch-Gordon coefficients which are determined by deriving the following relations (we use $|L, L_z; S, S_z\rangle$ convention for the product states of orbital and spin angular momentum):

$$\left|J=\frac{5}{2}, J_z=+\frac{3}{2}\right\rangle = +\sqrt{\frac{5}{7}}\left|3,+2;\frac{1}{2},-\frac{1}{2}\right\rangle - \sqrt{\frac{2}{7}}\left|3,+1;\frac{1}{2},+\frac{1}{2}\right\rangle, \tag{36a}$$
$$\left|J=\frac{5}{2}, J_z=-\frac{3}{2}\right\rangle = -\sqrt{\frac{5}{7}}\left|3,-2;\frac{1}{2},+\frac{1}{2}\right\rangle + \sqrt{\frac{2}{7}}\left|3,-1;\frac{1}{2},-\frac{1}{2}\right\rangle, \tag{36b}$$
$$\left|J=\frac{7}{2}, J_z=+\frac{3}{2}\right\rangle = +\sqrt{\frac{2}{7}}\left|3,+2;\frac{1}{2},-\frac{1}{2}\right\rangle + \sqrt{\frac{5}{7}}\left|3,+1;\frac{1}{2},+\frac{1}{2}\right\rangle, \tag{36c}$$
$$\left|J=\frac{7}{2}, J_z=-\frac{3}{2}\right\rangle = +\sqrt{\frac{2}{7}}\left|3,-2;\frac{1}{2},+\frac{1}{2}\right\rangle + \sqrt{\frac{5}{7}}\left|3,-1;\frac{1}{2},-\frac{1}{2}\right\rangle. \tag{36d}$$

From the above equations we obtain,

$$\langle 1|L_z+2S_z|1\rangle = -\langle 2|L_z+2S_z|2\rangle = \frac{9}{7}, \tag{37a}$$
$$\langle 3|L_z+2S_z|3\rangle = -\langle 4|L_z+2S_z|4\rangle = \frac{12}{7}, \tag{37b}$$
$$\langle 1|L_z+2S_z|3\rangle = \langle 3|L_z+2S_z|1\rangle = -\frac{\sqrt{10}}{7}, \tag{37c}$$
$$\langle 2|L_z+2S_z|4\rangle = \langle 4|L_z+2S_z|2\rangle = -\frac{\sqrt{10}}{7}. \tag{37d}$$

Using the above equations we find that,

$$\langle +|L_z+2S_z|+\rangle = 0.8615, \tag{38a}$$
$$\langle -|L_z+2S_z|-\rangle = -0.8615, \tag{38b}$$
$$\langle +|L_z+2S_z|-\rangle = \langle -|L_z+2S_z|+\rangle = -1.0784. \tag{38c}$$

Note that $\langle +|L_z+2S_z|-\rangle$ is not zero, unlike the case of the pure $J = 5/2$ ground state doublet considered previously. Using the above equations it immediately follows that the Zeeman term reduces to the form,

$$H_Z = -h_z(g_x s_x + g_z s_z). \tag{39}$$

when expressed in the subspace of the ground state doublet.

* ab12k@my.fsu.edu
† nevidomskyy@rice.edu
‡ hchanglani@fsu.edu

[1] Huang, Y.-P., Chen, G. & Hermele, M. Quantum spin ices and topological phases from dipolar-octupolar doublets on the pyrochlore lattice. *Physical Review Letters* **112**, 167203 (2014). URL https://link.aps.org/doi/10.1103/PhysRevLett.112.167203.

[2] Patri, A. S., Hosoi, M. & Kim, Y. B. Distinguishing dipolar and octupolar quantum spin ices using contrasting magnetostriction signatures. *Phys. Rev. Research* **2**, 023253 (2020). URL https://link.aps.org/doi/10.1103/PhysRevResearch.2.023253.

[3] Ross, K. A., Savary, L., Gaulin, B. D. & Balents, L. Quantum excitations in quantum spin ice. *Phys. Rev. X* **1**, 021002 (2011). URL https://link.aps.org/doi/10.1103/PhysRevX.1.021002.

[4] Gao, B. *et al.* Experimental signatures of a three-dimensional quantum spin liquid in effective spin-1/2 $Ce_2Zr_2O_7$ pyrochlore. *Nature Physics* **15**, 1052–1057 (2019). URL https://doi.org/10.1038/s41567-019-0577-6.

[5] Avella, A. & Mancini, F. (eds.). *Strongly Correlated Systems: Numerical Methods.* Springer Series in Solid-State Sciences (Springer Berlin Heidelberg, 2013). URL http://dx.doi.org/10.1007/978-3-642-35106-8.

[6] Changlani, H. Quantum versus classical effects at zero and finite temperature in the quantum pyrochlore $Yb_2Ti_2O_7$. Preprint at https://arxiv.org/abs/1710.02234v2 (2017).

[7] Keren, A. Dynamical simulation of spins on kagomé and square lattices. *Phys. Rev. Lett.* **72**, 3254–3257 (1994). URL https://link.aps.org/doi/10.1103/PhysRevLett.72.3254.

[8] Conlon, P. H. & Chalker, J. T. Spin dynamics in pyrochlore Heisenberg antiferromagnets. *Phys. Rev. Lett.* **102**, 237206 (2009). URL https://link.aps.org/doi/10.1103/PhysRevLett.102.237206.

[9] Zhang, S., Changlani, H. J., Plumb, K. W., Tchernyshyov, O. & Moessner, R. Dynamical structure factor of the three-dimensional quantum spin liquid candidate $NaCaNi_2F_7$. *Phys. Rev. Lett.* **122**, 167203 (2019). URL https://link.aps.org/doi/10.1103/PhysRevLett.122.167203.

[10] Savary, L. & Balents, L. Coulombic quantum liquids in spin-1/2 pyrochlores. *Phys. Rev. Lett.* **108**, 037202 (2012). URL https://link.aps.org/doi/10.1103/PhysRevLett.108.037202.

[11] Lee, S., Onoda, S. & Balents, L. Generic quantum spin ice. *Phys. Rev. B* **86**, 104412 (2012). URL https://link.aps.org/doi/10.1103/PhysRevB.86.104412.

[12] Benton, O., Jaubert, L. D. C., Singh, R. R. P., Oitmaa, J. & Shannon, N. Quantum spin ice with frustrated transverse exchange: From a π-flux phase to a nematic quantum spin liquid. *Phys. Rev. Lett.* **121**, 067201 (2018). URL https://link.aps.org/doi/10.1103/PhysRevLett.121.067201.

[13] Chen, G. Spectral periodicity of the spinon continuum in quantum spin ice. *Phys. Rev. B* **96**, 085136 (2017). URL https://link.aps.org/doi/10.1103/PhysRevB.96.085136.

[14] Sakurai, J. J. & Napolitano, J. J. *Modern Quantum Mechanics* (Pearson, 2010). URL https://books.google.com/books?id=qhi-QgAACAAJ.

[15] Sibille, R. *et al.* Experimental signatures of emergent quantum electrodynamics in $Pr_2Hf_2O_7$. *Nature Physics* **14**, 711–715 (2018). URL https://doi.org/10.1038/s41567-018-0116-x.